ORIGINAL ARTICLE

Wavelet denoising for quantum noise removal in chest digital tomosynthesis

Tsutomu Gomi · Masahiro Nakajima · Tokuo Umeda

Abstract

Purpose   Quantum noise impairs image quality in chest digital tomosynthesis (DT). A wavelet denoising processing algorithm for selectively removing quantum noise was developed and tested.

Methods   A wavelet denoising technique was implemented on a DT system and experimentally evaluated using chest phantom measurements including spatial resolution. Comparison was made with an existing post-reconstruction wavelet denoising processing algorithm reported by Badea et al. (Comput Med Imaging Graph 22:309–315, 1998). The potential DT quantum noise decrease was evaluated using different exposures with our technique (pre-reconstruction and post-reconstruction wavelet denoising processing via the balance sparsity-norm method) and the existing wavelet denoising processing algorithm. Wavelet denoising processing algorithms such as the contrast-to-noise ratio (CNR), root mean square error (RMSE) were compared with and without wavelet denoising processing. Modulation transfer functions (MTF) were evaluated for the in-focus plane. We performed a statistical analysis (multi-way analysis of variance) using the CNR and RMSE values.

Results   Our wavelet denoising processing algorithm significantly decreased the quantum noise and improved the contrast resolution in the reconstructed images (CNR and RMSE: pre-balance sparsity-norm wavelet denoising processing versus existing wavelet denoising processing, $P < 0.05$; post-balance sparsity-norm wavelet denoising processing versus existing wavelet denoising processing, $P < 0.05$; CNR: with versus without wavelet denoising processing, $P < 0.05$). The results showed that although MTF did not vary (thus preserving spatial resolution), the existing wavelet denoising processing algorithm caused MTF deterioration.

Conclusions   A balance sparsity-norm wavelet denoising processing algorithm for removing quantum noise in DT was demonstrated to be effective for certain classes of structures with high-frequency component features. This denoising approach may be useful for a variety of clinical applications for chest digital tomosynthesis when quantum noise is present.

Introduction

Digital tomosynthesis (DT) is a limited-angle image reconstruction method in which a projection dataset of a structure acquired at regular intervals during a single acquisition pass is used to reconstruct planar sections a priori. Tomosynthetic slices exhibit high resolution in planes parallel to the detector plane. Furthermore, DT provides the additional benefits of digital imaging [1–6] as well as the tomographic benefits of computed tomography (CT) at a decreased radiation dose and cost in an approach that is easily implemented in conjunction with chest radiography. This technique was developed by improving the older geometric tomography technique that has largely fallen out of favor for chest imaging because of the positioning difficulties, high radiation doses, and residual blur caused by out-of-plane structures. DT has overcome these difficulties by enabling the reconstruction of numerous image slices from a single low-dose image data acquisition.

T. Gomi (✉) · T. Umeda
School of Allied Health Sciences, Kitasato University, Kitasato,
1-15-1 Minami-ku, Sagamihara, Kanagawa252-0373, Japan
e-mail: gomi@kitasato-u.ac.jp

M. Nakajima
Hosoda Clinic, Tokyo, Japan

DT images are invariably affected by blurring because of out-of-plane structures and are superimposed on the focused fulcrum plane image by the limited acquisition angle. This can result in poor structure detectability in the in-focus plane.

DT reconstruction also suffers from "quantum noise" or inconsistent reconstructed images that suffer from a low signal-to-noise ratio (SNR) because of the superposition of several low-exposure projection images. Several methods have been proposed to suppress this irrelevant plane information and enhance the DT image quality, including sampling geometry optimization [7], pre-filtering projections [8–10], and post-processing of reconstructed images [6,11–14]. Post-processing can be further classified into 2 basic approaches: denoising through predictable noise reconstruction followed by subtraction from the tomographic images [11–14] and post-reconstruction filtering techniques that specifically address the artifact streaking that introduces tomosynthetic noise into DT images [6]. Obviously, no single method can be generally and effectively applied to all DT imaging cases. Reconstruction using inverse filtering yields images with few superimposed details, but a low spatial resolution along the rotational axis [8–10]. Noise reconstruction methods can be used to remove the noise attributed to all classes of structures. However, blurred out-of-plane structures must be removed from several planes [11–14], and the noise subtraction is associated with poor contrast in the resulting images because of the concurrent loss of plane-relevant details. In addition, post-reconstruction filtering techniques are only efficient for specific types of images [6].

Quantum mottle degrades radiographic images because of the spatial incident photon fluctuation. The lower the exposure, the more significant the quantum mottle will be in the image. Even if a perfect detector could be developed, the decrease in the patient dose would be restricted by the degree of quantum mottle. Therefore, new technology for noise removal that incorporates suitable processing is desired to further decrease the patient dose as well as improve the detector.

Wavelets have been widely used to analyze the characteristics of signals for irregular structures such as those often included in biomedical images. Therefore, it is entirely reasonable to analyze such signals using wavelets [15]. Donoho et al. developed a theoretical framework of discrete wavelet transforms to estimate signals degraded by additive noise in their wavelet shrinkage method [16]. This method has been used for denoising because of its simplicity and effectiveness. A previous study investigated the use of this method for 2-dimensional tomography reconstruction [17], and other modalities [18,19]. However, appropriate threshold estimation is often difficult and a priori knowledge of the noise intensity is necessary to determine the optimal threshold. Furthermore, the signal edge information might be removed during this denoising process. Badea et al. developed a wavelet

that could be applied to the reconstructed plane for DT [20]. This technique was developed to discriminate and subsequently remove unrelated structures from the reconstructed plane. In Badea's wavelet approach, thresholding is based on location; the local maxima that account for the blurred edges are discarded inside the noise map created at each wavelet scale. However, the effect of this technique on large structures is limited to further blurring with incomplete residual noise removal.

To resolve the incomplete residual noise removal, we suggest a balance sparsity-norm [21–23] wavelet denoising processing method. The balance sparsity-norm method produces a calculated norm of the spectrum, which balances thresholding with loss in image quality. The novel aspect of our technique is that it is a hybrid method that exploits both the predictability of quantum noise generation and the signal locality of the wavelet domain. Therefore, we anticipate that both the conserved spatial resolution and an effective quantum noise reduction will be achieved with the balance sparsity-norm technique. Against this background, we developed a wavelet-based method using a balance sparsity-norm algorithm to generate reconstructed images that would conserve spatial resolution and effectively decrease the quantum noise. Nodule lesion detection tends to be difficult because of the effects of quantum noise in chest imaging [24–26]. Accordingly, this algorithm is intended only for the chest DT field.

The developed DT technique has been used to conduct diagnostic studies in hospitals, where it enables the visualization of fine body structures with a shorter scan time. Despite these merits, all DT systems present the problem of exposing patients to radiation. Therefore, it becomes necessary to remove the noise in order to improve the DT image quality.

This study discusses a novel balance sparsity-norm wavelet denoising algorithm for chest DT to selectively remove quantum noise structures and possibly improve the image quality improvement and compares this method with the existing Badea algorithm. The method was implemented on a DT system and experimentally evaluated using chest phantom measurements and spatial resolution. In this paper, we evaluated the possibility that this balance sparsity-norm wavelet denoising algorithm would enhance the clinical applications of chest DT in medical imaging fields, where such structures (i.e., those that improve nodule detection) are foci of interest.

Materials and methods

Tomosynthesis system

The DT system (SonialVision Safire II; Shimadzu Co., Kyoto, Japan) comprised an X-ray tube with a 0.4-mm focal

spot and a 362.88×362.88-mm digital flat-panel detector composed of amorphous selenium. The size of each detector element was 150×150 µm. Tomography was performed using a linear tomographic movement, a total acquisition time of 6.4 s, and an acquisition angle of 40°. Projection images were sampled during a single tomographic pass (74 projections), using a matrix size of $1,440 \times 1,440$ with 12 bits per image, and were used to reconstruct tomograms of a desired height. Reconstructed images (0.252 mm/pixel) were obtained at a 5-mm slice thickness and 5-mm reconstruction intervals. An anti-scatter grid was used (focused type; grid ratio 12:1). The distance from the source to the isocenter was 980 mm and that from the isocenter to the detector was 1,100 mm (3.0-mm aluminum equivalent filtration). The DT images were reconstructed using filtered backprojection with the conventional Shepp–Logan filter kernel. Image reconstruction processing from real DBT system projection data was performed using MATLAB 8.2.0.701 (Mathworks, Natick, MA, USA) [27].

Noise differentiation

Two types of noise are apparent in tomography images [28]. One type is due to electrical noise or quantization (round-off) errors, and the other is due to x-ray photon fluctuations. Because our study aimed to improve image quality, we disregarded the low electric noise [29–31] and considered only quantum mottle (quantum noise), which is caused by X-ray photon fluctuation.

We denoted the intensity of the incident X-rays as $I_0(x, y)$ and that of the X-rays that passed through the structure at the location (x, y) as $I(x, y)$. The image data $f(x, y)$ were calculated as follows:

$$f(x, y) = ln \frac{I_0(x, y)}{I(x, y)} \qquad (1)$$

The randomness of $I(x_0, y_0)$ at the location (x_0, y_0) was statistically described by the Poisson probability function as

$$p\{I(x_0, y_0)\} = \frac{\left[\bar{I}(x_0, y_o)^{I(x_0, y_0)}\right]}{I(x_0, y_0)!} e^{-\bar{I}(x_0, y_o)}, \qquad (2)$$

where $p\{.\}$ denotes the probability and $\bar{I}(x_0, y_0)$ denotes the expected value of the measurement. In addition, $\bar{I}(x_0, y_0) = E\{I(x_0, y_0)\}$, where $E\{.\}$ denotes the statistical expectation. Given the randomness of I, the measured image $f(x, y)$ differs from the true value. The error is the noise due to X-ray photon fluctuation.

Wavelet denoising processing

In recent years, wavelet theory has been extensively studied as a promising tool with which to decrease quantum noise. We used a 2-dimensional discrete wavelet algorithm in this

study [32]. The approximate function for level j of an image $f(x, y)$ was expressed using Eq. 3 along the x-direction and the linear sum of a scaling function along the y-direction, as follows:

$$f_j(x, y) = \sum_k \sum_l c_{LL,k,l}^{(j)} \phi\left(2^j x - k\right) \phi\left(2^j y - l\right) \qquad (3)$$

where ϕ is a scaling function. An expansion coefficient of the function $c_{LL,k,l}^{(j)}$ in Eq. 3 was used to analyze Eq. 4 in the decomposition algorithm. An image is divided into smoothing (LL), horizontal (HL), vertical (LH), and diagonal images (HH) during processing using the decomposition algorithm as follows:

$$c_{LL,k,l}^{(j-1)} = \sum_n \sum_m \frac{1}{2} g_{2k-n} \frac{1}{2} g_{2l-m} c_{LL,m,n}^{(j)} \qquad (4)$$

$$c_{HL,k,l}^{(j-1)} = \sum_n \sum_m \frac{1}{2} h_{2k-n} \frac{1}{2} g_{2l-m} c_{LL,m,n}^{(j)} \qquad (5)$$

$$c_{LH,k,l}^{(j-1)} = \sum_n \sum_m \frac{1}{2} g_{2k-n} \frac{1}{2} h_{2l-m} c_{LL,m,n}^{(j)} \qquad (6)$$

$$c_{HH,k,l}^{(j-1)} = \sum_n \sum_m \frac{1}{2} h_{2k-n} \frac{1}{2} h_{2l-m} c_{LL,m,n}^{(j)}, \qquad (7)$$

where L indicates the low-frequency components and H indicates the high-frequency components.

This algorithm transforms a wavelet into an image at each level by repeating the division for a smoothing image. Furthermore, the algorithm resolves an image into a differently scaled image (corresponding to frequency) via wavelet transformation and transforms the expansion coefficients $c_{LL,k,l}^{(j)}$, $c_{HL,k,l}^{(j)}$, $c_{LH,k,l}^{(j)}$, and $c_{HH,k,l}^{(j)}$, as shown in Eqs. 8–11, by image processing of the wavelet process W.

$$\hat{c}_{LL,k,l}^{(j)} = W_{LL}^{(j)}\left(c_{LL,k,l}^{(j)}\right) \qquad (8)$$

$$\hat{c}_{HL,k,l}^{(j)} = W_{HL}^{(j)}\left(c_{HL,k,l}^{(j)}\right) \qquad (9)$$

$$\hat{c}_{LH,k,l}^{(j)} = W_{LH}^{(j)}\left(c_{LH,k,l}^{(j)}\right) \qquad (10)$$

$$\hat{c}_{HH,k,l}^{(j)} = W_{HH}^{(j)}\left(c_{HH,k,l}^{(j)}\right) \qquad (11)$$

Next, a wavelet transformation processing image $\hat{f}(x, y)$ is reconstructed from Eq. 12.

$$\hat{f}(x, y) = \sum_{j=1}^{J} \left[\sum_k \sum_l \hat{c}_{HL,k,l}^{(-l)} \psi\left(2^j x - k\right) \phi\left(2^j y - l\right) \right.$$
$$+ \sum_k \sum_l \hat{c}_{LH,k,l}^{(-l)} \phi\left(2^j x - k\right) \psi\left(2^j y - l\right)$$
$$\left. + \sum_k \sum_l \hat{c}_{HH,k,l}^{(-l)} \psi\left(2^j x - k\right) \psi\left(2^j y - l\right) \right]$$
$$+ \sum_k \sum_l \hat{c}_{LL,k,l}^{(-l)} \phi\left(2^{-J} x - k\right) \phi\left(2^{-J} y - l\right)$$
$$\qquad (12)$$

where ψ is a wavelet function. Daubechie's mother wavelet function was used [33] (coefficient: 2, level: 5).

The denoising method used in this study was based on balance sparsity-norm [21,22] thresholding [23], in order to determine the appropriate threshold for the image wavelet coefficients for denoising in the MATLAB wavelet toolbox 4.8 (Mathworks, Natick, MA, USA) [34]. The threshold value for this expansion coefficient is given by Eq. 13.

$$\hat{c}_{p,k,l}^{(j)} = \begin{cases} 0 & \left| c_{p,k,l}^{(j)} \right| < T_h \\ c_{p,k,l}^{(j)} & \left| c_{p,k,l} \right| \geq T_h \end{cases}, \qquad (13)$$

where $p = \{LL, HL, LH, HH\}$ and T_h is a threshold value.

Because we simply want to calculate how much total power is lost in the image, a simpler heuristic will work well and be much easier to compute. To find the right balance, we should calculate the norm of the image's Fourier spectrum for uniformly distributed threshold values between 0 and 1. At a threshold of 0, the percent number of zeros should be near 0 % and the percent norm should be 100 %. However, at a threshold of 1, we would expect the percent zeros to be 100 % and the percent norm to be 0 %. Therefore, the curves of the 2 quantities intersect at some point, and we can set the global threshold to be at this intersection. As a result, the intersection point of the 2 curves in Fig. 1 can be used to set the selective different global threshold.

In addition, we recognize that a loss of coefficients at the lower decomposition levels exerts a much greater impact on the image quality than that of coefficients at higher decomposition levels. A solution is to only decompose the image to a certain level instead of decomposing the image to the last level. Wavelet reconstruction excludes the quantum noise component (level 1) and uses image processing at levels 2–5. We processed the images by calculating the threshold value according to the balance sparsity-norm method (Figs. 1, 2).

Evaluation methods

Contrast-to-noise ratio (CNR) and root mean square error (RMSE)

The chest phantom N1 (Kyoto Kagaku Co., Tokyo, Japan) comprises soft tissue and vessels composed of polyurethane, epoxy resin, and calcium carbonate. The artificial ground-glass opacity-type pulmonary nodules measured 8 mm in diameter and were composed of homogenous urethane foam. These were arranged in each lung region, and the nodules adjacent to the edges of the lungs or mixed with blood vessels were chosen. The target contrast (ΔCT) values of the artificial pulmonary nodules [ΔCT = 200 Hounsfield units (HU)] were determined on the basis of the artificial lung parenchymal background.

Each projection image was acquired with the following parameters: reference exposure, 120 kVp, 160 mA; exposure time, 3.2 ms; standard exposures, 25 mA and 1.6 ms; and low-exposure, 10 mA and 1.4 ms. The exposure established
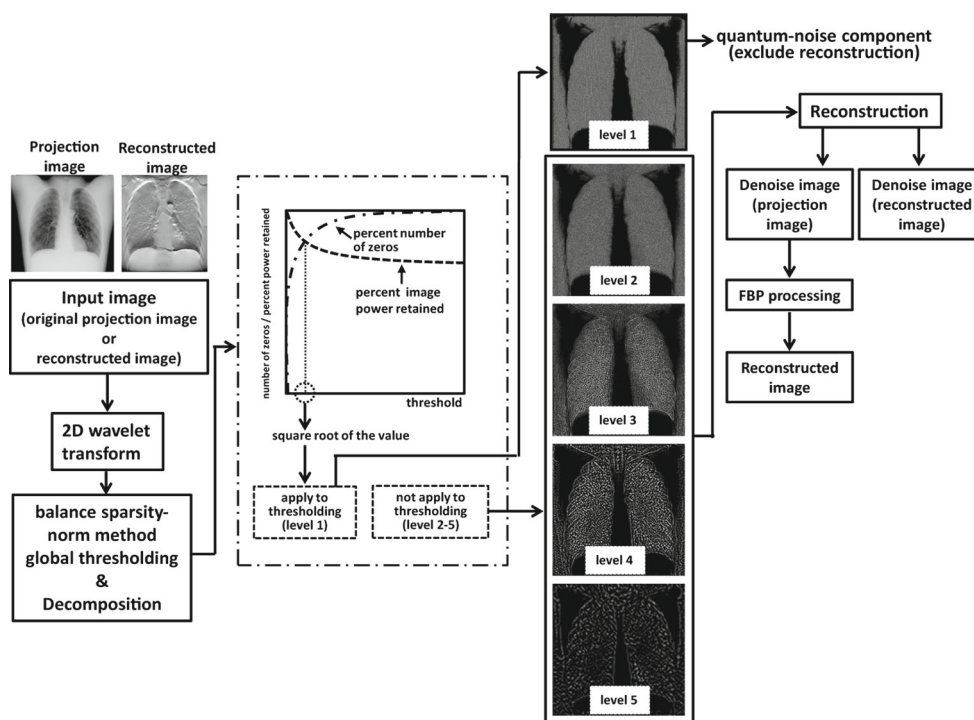
Fig. 1 Flow chart illustrating the successive steps in the balance sparsity-norm wavelet processing method

Fig. 2 Flow chart illustrating
the successive steps in the
wavelet processing method
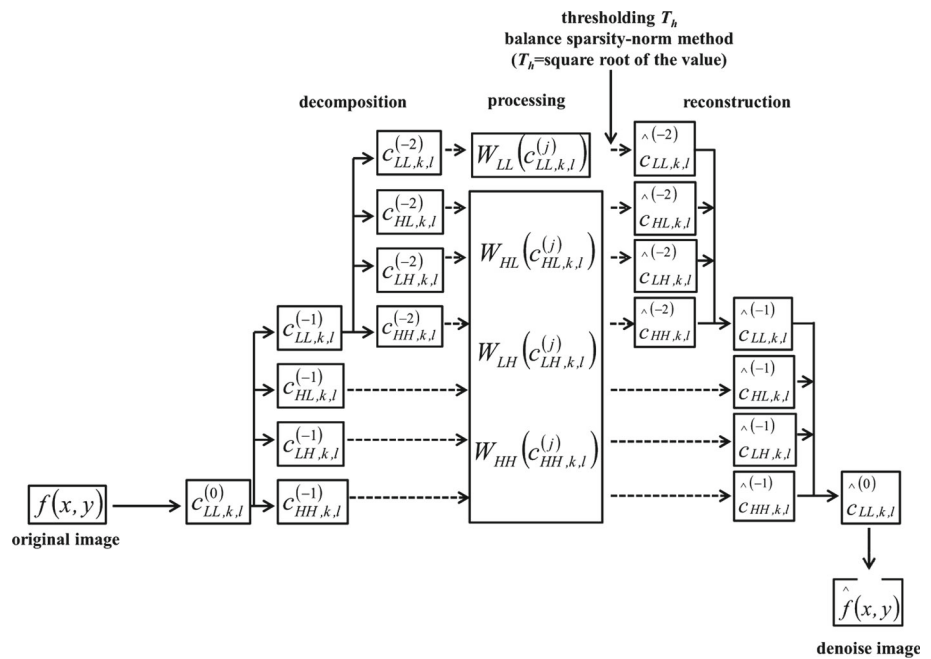
the chest scan conditions reported by Yamada et al. [35] as the standard (effective dose: 0.215 mSv). We calculated the effective dose for each exposure condition using Monte Carlo-based software (PCXMC version 2.0; Radiation and Nuclear Safety Authority, Helsinki, Finland) [36]. PCXMC was used to simulate the absorbed dose in the phantom and determine the effective dose. Absorbed doses were measured for the X-ray tube output using a glass dosimeter (AGC Techno Glass Co., Chiba, Japan; materials: GD-352M). Different exposure conditions were compared, including those with and without wavelet denoising processing. The potential reduction in quantum noise with DT was verified using different imaging exposures for the artificial chest phantom pulmonary nodules. Additionally, we compared the performance of pre-reconstruction and post-reconstruction wavelet denoising processing (balance sparsity-norm: pre-reconstruction and post-reconstruction processing; existing Badea algorithm: post-reconstruction processing). Pre-reconstruction processing uses defined wavelet denoising for the projected image whereas post-reconstruction processing uses defined wavelet denoising for the reconstructed image. The balance sparsity-norm post-reconstruction algorithm was identical to that of the pre-reconstruction but was only applied post-reconstruction. The effects of the wavelet denoising processing techniques were evaluated for the in-focus plane in terms of the CNR, RMSE (comparison between with and without wavelet denoising processing), and modulation transfer function (MTF).

CNR was defined as $\frac{N_1 - N_0}{\sigma_0}$, where N_1 is the mean pixel value in the structure, N_0 is the mean pixel value in the background area, and σ_0 is the standard deviation of the pixel

values in the background. σ_0 not only includes the photon statistics and electronic noise in the results but also structural noise that could obscure the structure.

RMSE is defined as

$$RMSE = \sqrt{\frac{\sum_{i=1}^{n} (\hat{y}_k - y_k)^2}{n}}, \qquad (14)$$

where y_k is the observed image, $\hat{y}_k$ is the referenced image, and n is the number of compounds in the analyzed set.

Spatial resolution

The line-spread function (LSF) in the scan plane is frequently employed to characterize tomographic spatial resolution, and MTF can be derived from LSF [37]. The spatial resolution evaluation used the reconstructed wire image (0.252 mm/pixel). We designed experimental conditions in which a copper wire (0.89 mm in diameter) was inserted into the center of a polymethyl methacrylate cube (200 × 200 × 200 mm). The wire was arranged perpendicularly to the mid-detector position in the sweep direction. The wire length was larger than the detector dimensions to eliminate impact from the structure's edge. The reconstructed wire image was used on an in-focus plane. The corresponding output was calculated by multiplying each line source in the intensity distribution of structures by the convolution LSF. MTF was obtained from a 1-dimensional Fourier transformation of the convolution LSF. The different exposure conditions, including those with and without wavelet denoising processing, were compared. The MTF degradation (or its absence) was evaluated at different imaging dose levels. Additionally, we compared the

performances of pre-reconstruction and post-reconstruction wavelet denoising processing (balance sparsity-norm: pre-reconstruction and post-reconstruction processing; existing Badea algorithm: post-reconstruction processing).

Statistical analysis

The effects of image denoising were assessed in a multi-way analysis of variance. Statistical tests were used to assess differences between the CNR and RMSE values of the balance sparsity-norm and existing Badea algorithms (Tukey–Kramer test) with and without wavelet denoising processing (F test). We analyzed the tests with a total of 5 samples. The statistical analysis was performed using SPSS for Windows, version 21.0 (SPSS Inc., Chicago, IL, USA). All probability (P) values of <0.05 were considered significant.

Results

We compared the CNR and RMSE of the reconstructed images obtained using 2 different exposure conditions with and without wavelet denoising processing (Figs. 3, 4, 5 and Table 1). In addition, the intensity profiles along the sweep direction with the wavelet denoising processing were investigated (Figs. 6, 7). The wavelet denoising processing effectively decreased the quantum noise in the reconstructed images obtained with pre-reconstruction and post-reconstruction wavelet denoising processing (balance sparsity-norm). Furthermore, with balance sparsity-norm wavelet denoising processing, the contrast detectability was high relative to that of the existing Badea algorithm. In the reconstructed images obtained from all wavelet denoising processing techniques, the quantum noise structure was reduced in the low- and standard-exposure images and the noise structure was slightly smoothed (Figs. 6, 7 and Table 1). In the reconstructed images obtained with the existing Badea algorithm, the noise structure was reduced and smoothed and the normal structure was not preserved (Figs. 5, 6, 7 and Table 1).

The contrast detectability difference with and without wavelet denoising processing was statistically significant [$P < 0.05$, $F(1, 51) = 60.290$, mean square $= 6.501$]. The

Fig. 3 Comparison of the reconstructed and subtracted region of interest (ROI) images using pre-reconstruction wavelet processing with different exposures (X-ray sweep direction: *vertical direction*). **a** Reference image (2.752 mSv); **b** standard-dose image (0.215 mSv); **c** standard-dose image with wavelet denoising processing (0.215 mSv); **d** difference between (**b**) and (**c**) (0.215 mSv); **e** low-dose image (0.075 mSv); **f** low-dose image with wavelet denoising processing (0.075 mSv); **g** difference between (**e**) and (**f**) (0.075 mSv)
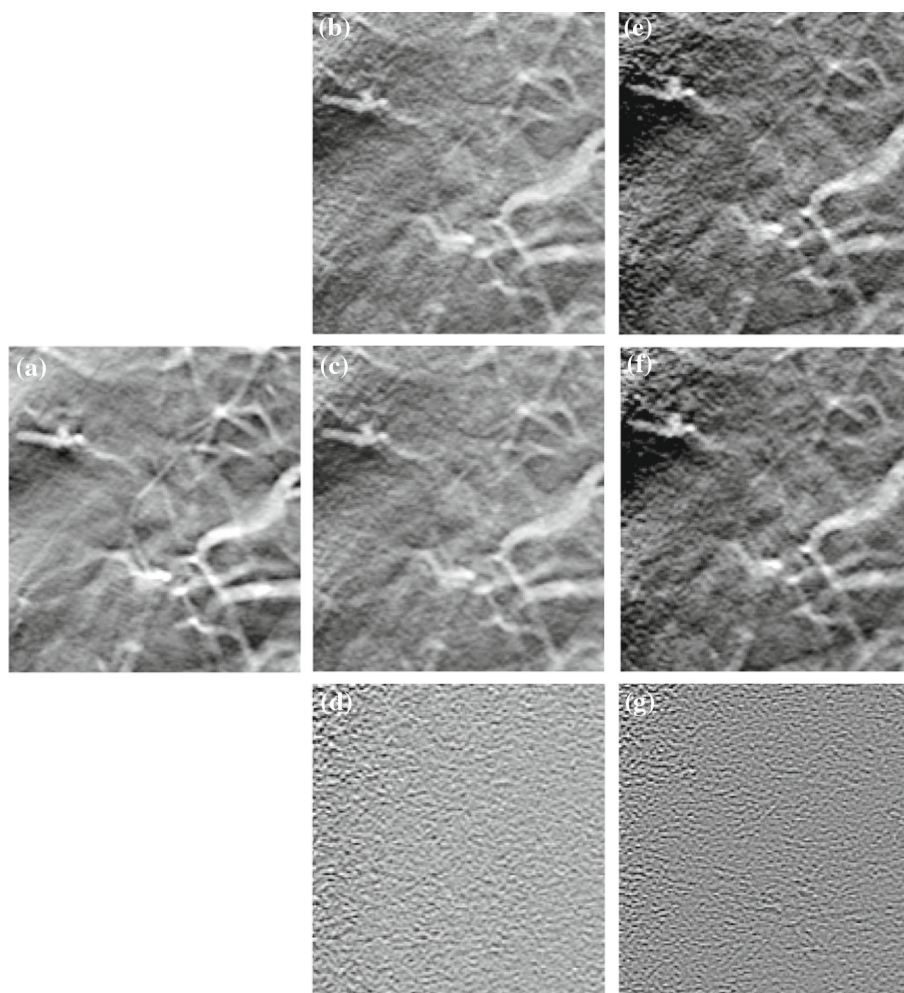
Fig. 4 Comparison of the reconstructed and subtracted region of interest (ROI) images using post-reconstruction wavelet processing with the balance sparsity-norm method for different exposures (X-ray sweep direction: vertical direction). (**a**) Reference image (2.752 mSv); (**b**) standard-dose image (0.215 mSv); (**c**) standard-dose image with wavelet denoising processing (0.215 mSv); (**d**) difference between (**b**) and (**c**) (0.215 mSv); (**e**) low-dose image (0.075 mSv); (**f**) low-dose image with wavelet denoising processing (0.075 mSv); (**g**) difference between (**e**) and (**f**) (0.075 mSv)
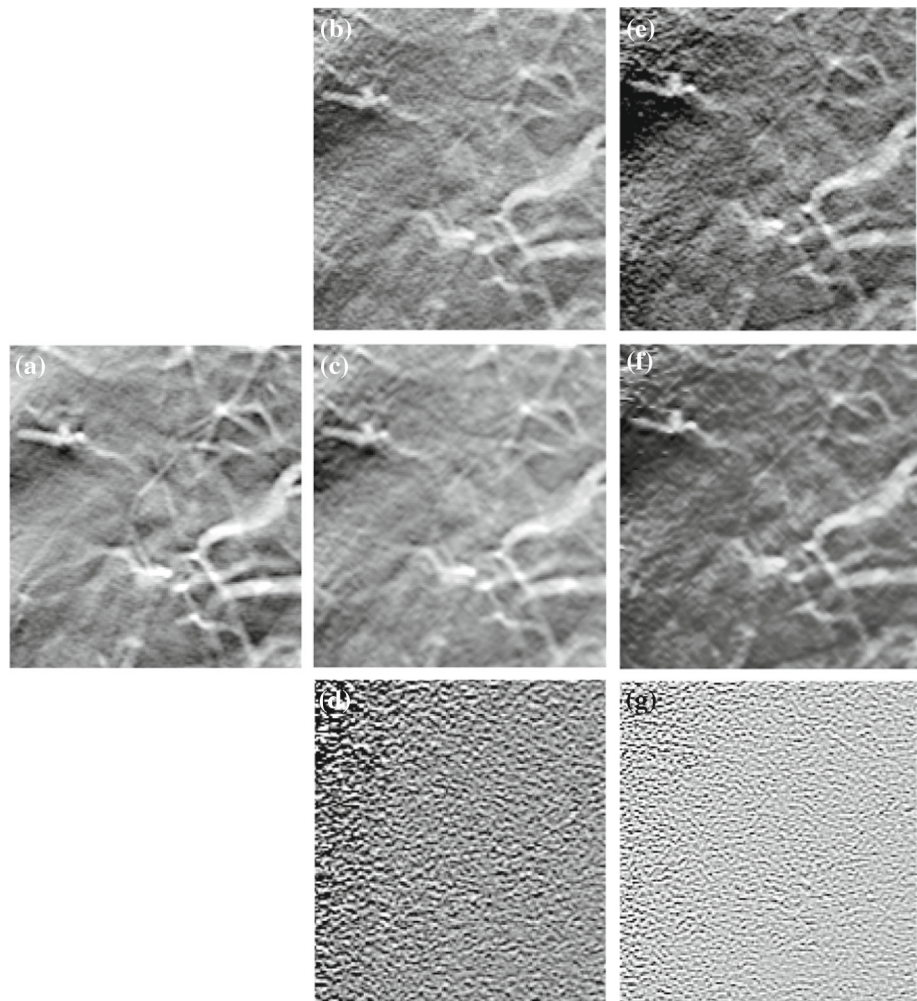
contrast detectability difference between pre-reconstruction with the balance sparsity-norm technique and the existing Badea algorithm was statistically significant [$P < 0.05$, 95 % confidence interval (CI): 0.029–0.530]. The contrast detectability difference between post-reconstruction with the balance sparsity-norm technique and the existing Badea algorithm was also statistically significant ($P < 0.05$, 95 % CI: 0.156–0.658). The contrast detectability difference between pre-reconstruction and post-reconstruction with the balance sparsity-norm technique was not statistically significant ($P = 0.442$, 95 % CI: -0.378 to 0.123]). The image error difference between pre-reconstruction and post-reconstruction with the balance sparsity-norm technique was not statistically significant ($P = 0.494$, 95 % CI: -0.001 to 0.002). The image error difference between pre-reconstruction with the balance sparsity-norm technique and the existing Badea algorithm was statistically significant ($P < 0.05$, 95 % CI: -0.016 to -0.012). The image error difference between post-reconstruction with the balance sparsity-norm technique and the existing Badea algorithm was statistically significant ($P < 0.05$, 95 % CI: -0.017 to -0.013).

Regarding the MTF results, the spatial resolution was higher in the reference dose images with high-frequency bands and lower in the post-reconstruction wavelet denoising processing images (existing Badea algorithm) bands of all frequencies. Deteriorated spatial resolution was accepted with post-reconstruction wavelet denoising processing (existing Badea algorithm, Fig. 8). These results suggest that the image quality could be improved by using the post-reconstruction wavelet denoising balance sparsity-norm method.

Discussion

Our experimental results clearly demonstrate the ability of balance sparsity-norm pre-reconstruction and post-reconstruction wavelet denoising processing to remove quantum noise from chest DT images. In this study, the in-focus plane intensities of the normal structures remained unchanged, whereas the superimposed quantum noise was removed and replaced with the average background inten-

Fig. 5 Comparison of the reconstructed and subtracted region of interest (ROI) images using post-reconstruction wavelet processing with the Badea algorithm for different exposures (X-ray sweep direction; *vertical direction*). **a** Reference image (2.752 mSv); **b** standard image (0.215 mSv); **c** standard image with wavelet denoising processing (0.215 mSv); **d** difference between (**b**) and (**c**) (0.215 mSv); **e** low-dose image (0.075 mSv); **f** low-dose image with wavelet denoising processing (0.075 mSv); **g** difference between (**e**) and (**f**) (0.075 mSv)
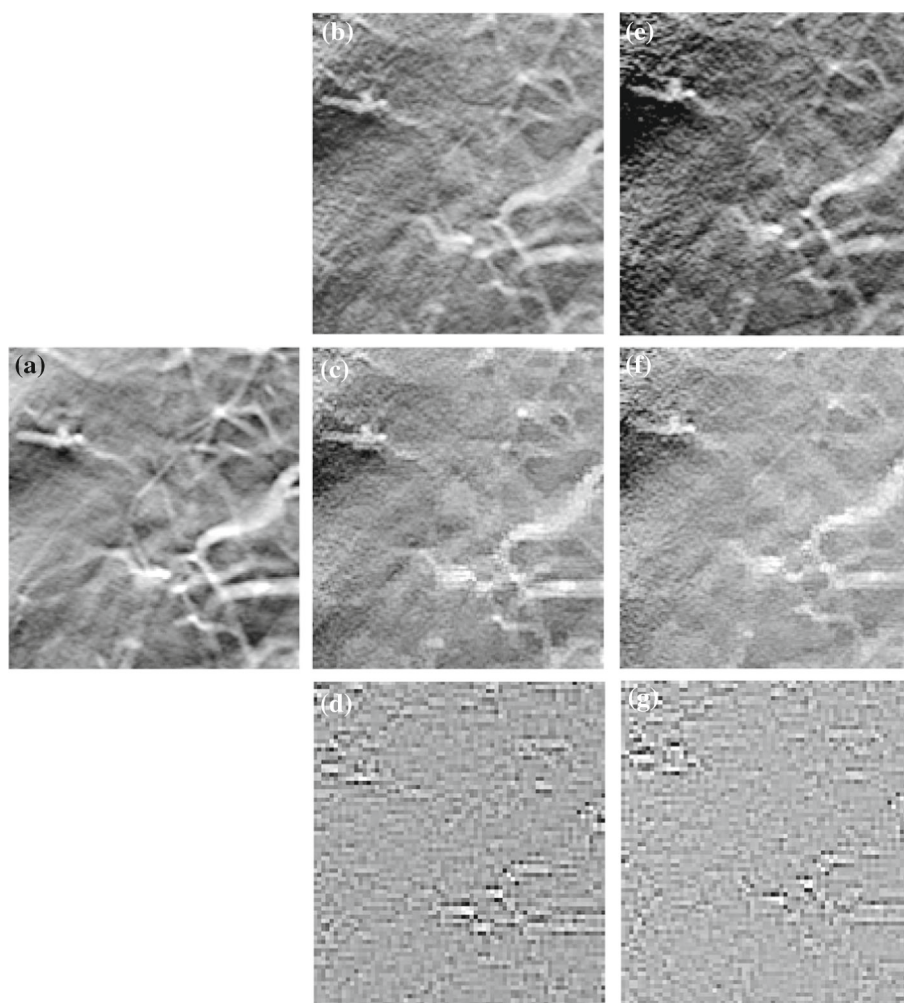
sity level. MTF preserved the spatial resolution using balance sparsity-norm pre-reconstruction and post-reconstruction wavelet denoising processing.

However, the influence of the Badea algorithm on low-dose exposure patterns was limited to incomplete residual quantum noise removal. The selective behavior of this technique was expected because the last wavelet decomposition approximation actually contained background alone; therefore, the undesirable superimposed structures were effectively removed by eliminating the local maxima that accounted for the quantum noise [20]. However, the large structures constituted low-frequency elements and could be filtered because they were present in the coarse wavelet transformation approximations.

Balance sparsity-norm pre-reconstruction and post-reconstruction wavelet denoising processing could successfully eliminate in-focus plane denoising. However, on a heterogeneous background, balance sparsity-norm pre-reconstruction and post-reconstruction wavelet denoising processing could not achieve good CNR values for the artificial pulmonary nodules with high inherent CNR. The slightly

higher CNR values for post-reconstruction wavelet denoising processing, compared with those for pre-reconstruction wavelet denoising processing, can be explained by the inevitable use of limited scanning arcs and the enhanced high-frequency component of the reconstruction kernel filter. We recommend the post-reconstruction wavelet denoising processing technique when considering the access to image processing and image quality (e.g., a slightly higher CNR).

Noise removal during post-reconstruction wavelet denoising processing is attained by subtracting the noise mask from the DT reconstruction plane; this noise mask is the sum of the restored set of all blurred replicas in the DT plane, weighted accordingly.

Therefore, this sum contains the image that has been added as quantum noise to the plane of interest. However, it also contains a directionally blurred version of the tomogram of interest. The effect of this blurred post-noise mask subtraction version is similar to the effect of unsharpened filters such that the edges of the reconstructed structures in the plane of interest are enhanced in the direction of the line intersecting the tomogram with the trajectory plane.

Table 1 Comparison of the contrast-to-noise ratio (CNR) and root mean square error (RMSE) values using pre- and post-reconstruction wavelet processing for different exposures

	CNR	
	Without wavelet denoise	With wavelet denoise
Reference dose (2.752 mSv)	5.97	–
Pre-reconstruction processing with balance sparsity-norm		
Standard dose (0.215 mSv)	4.18	5.46
Low dose (0.075 mSv)	1.01	1.25
Post-reconstruction processing with balance sparsity-norm		
Standard dose (0.215 mSv)	4.18	5.69
Low dose (0.075 mSv)	1.01	1.53
Post-reconstruction processing with Badea algorithm		
Standard dose (0.215 mSv)	4.18	4.30
Low dose (0.075 mSv)	1.01	1.29
RMSE (without vs. with wavelet denoise)		
Pre-reconstruction processing with balance sparsity-norm		
Standard dose (0.215 mSv)	0.0039	
Low dose (0.075 mSv)	0.0092	
Post-reconstruction processing with balance sparsity-norm		
Standard dose (0.215 mSv)	0.0058	
Low dose (0.075 mSv)	0.0055	
Post-reconstruction processing with Badea algorithm		
Standard dose (0.215 mSv)	0.0181	
Low dose (0.075 mSv)	0.0247	

In all wavelet denoise processing techniques, the quantum noise structure was decreased with the low and standard-exposure images. The balance sparsity-norm wavelet denoise processing; the contrast detectability was high in comparison with existing Badea algorithm

Fig. 6 Comparison of the intensity profiles of different exposures. **a** Intensity profiles using original, pre-, and post-reconstruction wavelet processing at different exposures (2.752 vs. 0.215 mSv); **b** intensity profiles using original, pre-, and post-reconstruction wavelet processing at different exposures (2.752 vs. 0.075 mSv)
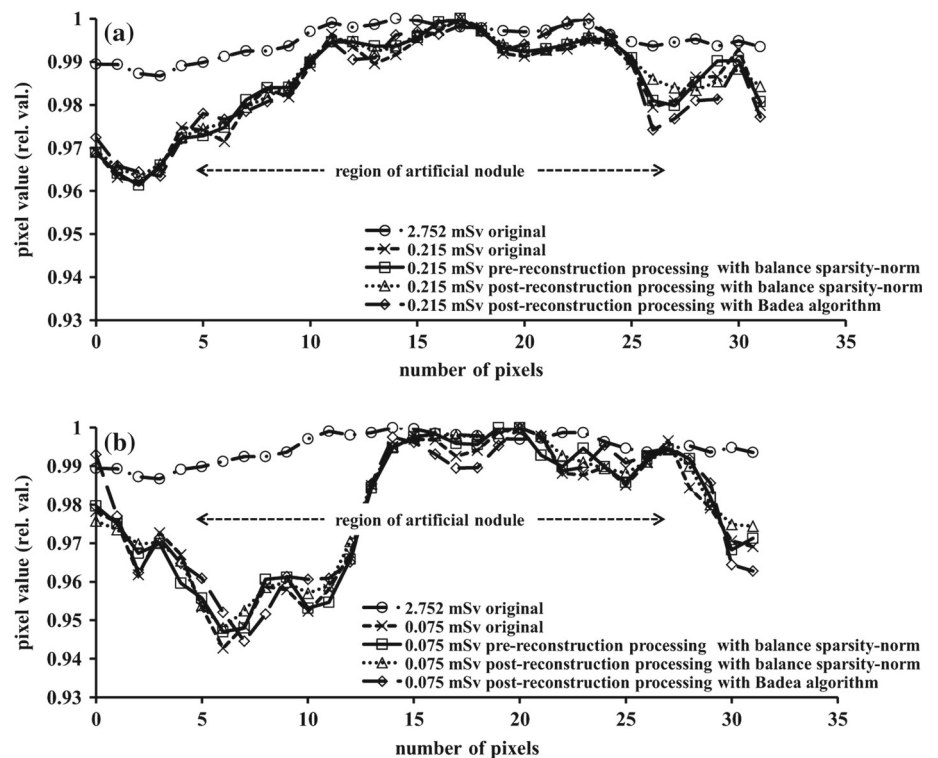
Fig. 7 Zoomed intensity profiles that correspond with Fig. 5. Quantum noise was removed while preserving the normal structures using pre-reconstruction wavelet processing. **a** Intensity profiles using pre-reconstruction and post-reconstruction wavelet processing at 0.215 mSv; **b** intensity profiles using pre-reconstruction and post-reconstruction wavelet processing at 0.075 mSv
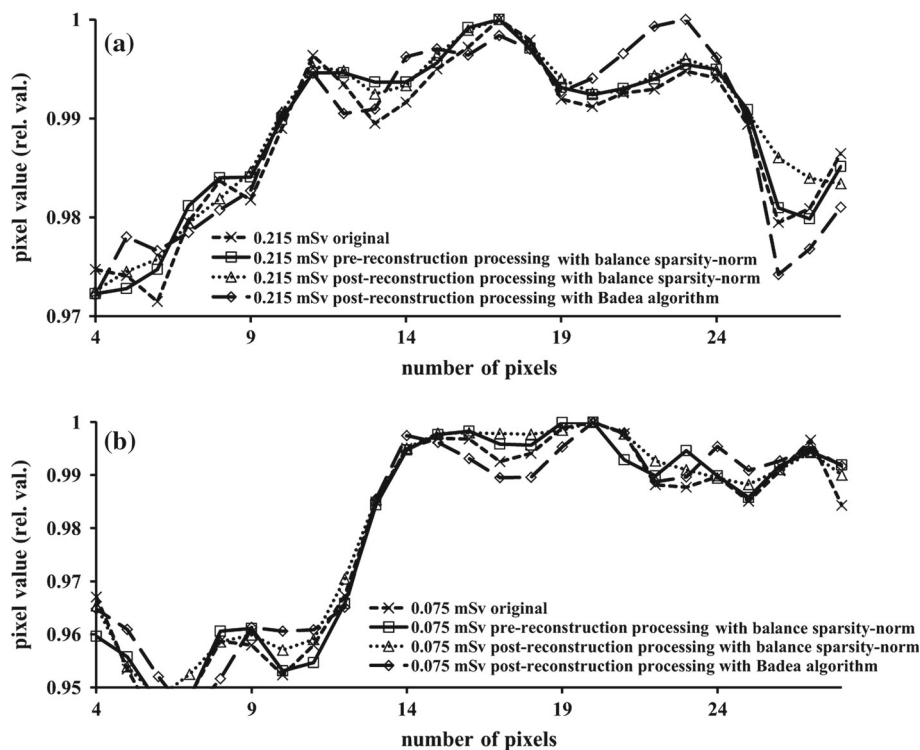
Fig. 8 Comparison of the modulation transfer function (MTF) at different exposures. **a** MTF using the original, pre-, and post-reconstruction wavelet processing methods at different exposures (2.752 vs. 0.215 mSv); **b** MTF using the original, pre-, and post-reconstruction wavelet processing methods at different exposures (2.752 vs. 0.075 mSv)
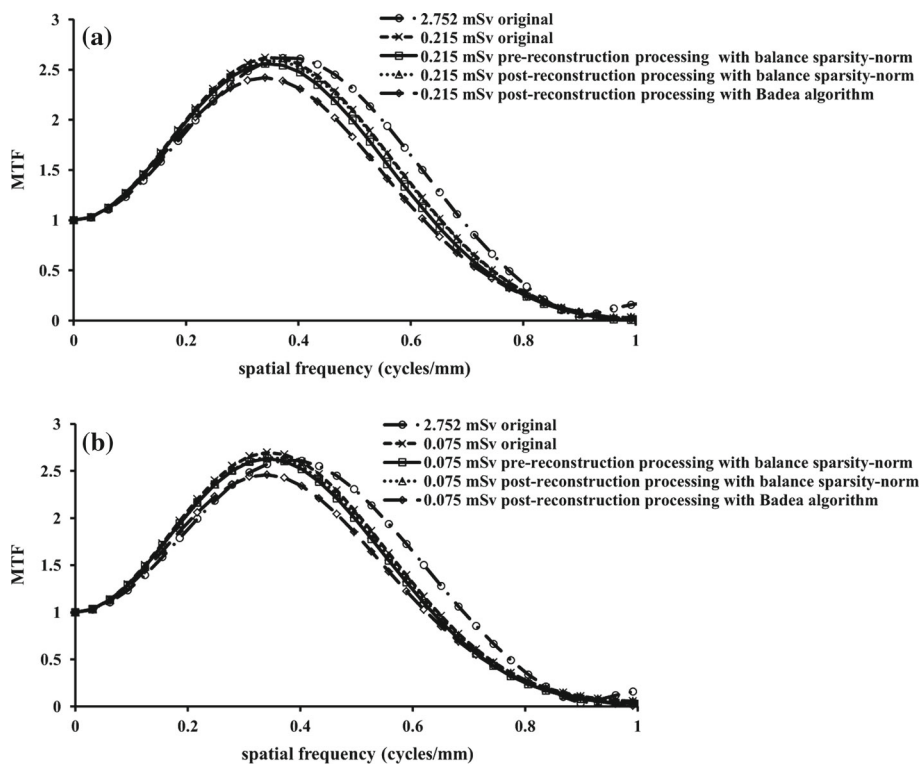
Quantum noise plays an important role in radiograph contrast resolution degradation. This noise increases by 1/sqrt (exposure) with X-ray exposure and constitutes the dominant noise source at low radiation exposure levels. Because of quantum noise, the technical factors used to decrease the radiation doses in the DT system are limited to levels usually employed in conventional tomography. However, for cases in which the presence of quantum noise is not an issue, tomograms can be obtained with the technical specifications used for radiography. DT provides 3-dimensional imaging at a

dose level comparable with a 2-view chest X-ray examination and might therefore provide a low-dose alternative to thoracic CT for obtaining depth information during chest imaging [38]. Moreover, DT can overcome the difficulties of geometric tomography by enabling the reconstruction of numerous image slices from a single low-dose image data acquisition.

Our balance sparsity-norm post-reconstruction wavelet denoising processing technique has therefore been appropriately applied to captured still tomosynthesis images to enhance visualization and, mainly, to improve the image quality in a 2-dimensional space. Our balance sparsity-norm wavelet denoising processing technique showed superior image characteristics (high contrast, decreased noise, and preserved spatial resolution) in comparison with an existing Badea algorithm, indicating a possible improvement in clinical diagnosis accuracy. Furthermore, this technique may decrease the dose without causing a deterioration in image quality. Accordingly, this technique is particularly important for both chest imaging and radiotherapy imaging techniques (e.g., image-guided radiotherapy), in which a high level of accuracy with respect to tumor localization is of primary importance.

Conclusion

A balance sparsity-norm pre-reconstruction and post-reconstruction wavelet denoising processing technique was developed as a novel technique to detect and subsequently remove quantum noise in the context of chest DT. This technique preserved the spatial resolution and effectively removed the quantum noise. The approach exploited a priori knowledge regarding quantum noise production. Quantum noise was removed through wavelet coefficient thresholding, followed by inverse reconstruction. This approach involved a wavelet technique specifically for chest DT images and has been demonstrated to effectively remove quantum mottle noise from chest DT images of structures with features of high-frequency components. Furthermore, this approach suggests the possibility that the image quality could be improved. Therefore, we believe that this technique will enhance the clinical applications of chest DT in medical imaging fields, in which such structures are a focus of interest.

References

1. Dobbins JT, Mcadams HP, Song JW et al (2008) Digital tomosynthesis of the chest for lung nodule detection: interim sensitivity results from an ongoing HIH-sponsored trial. Med Phys 35:2554–2557
2. Vikgren J, Zachrisson S, Svalkvist A et al (2008) Tomosynthesis: comparison of chest tomosynthesis and chest radiography for detection of pulmonary nodules: human observer study. Radiology 249:1034–1041
3. Quaia E, Baratella E, Cioffi V et al (2010) The value of digital tomosynthesis in the diagnosis of suspected pulmonary lesions on chest radiography. Acad Radiol 17:1267–1274
4. Lee G, Jeong YJ, Kim KI et al (2013) Comparison of chest digital tomosynthesis and chest radiography for detection of asbestos-related pleuropulmonary disease. Clin Radiol 68:376–382
5. Sone S, Kasuga T, Sakai F et al (1991) Development of a high-resolution digital tomosynthesis system and its clinical application. Radiographics 11:807–822
6. Sone S, Kasuga T, Sakai F et al (1995) Image processing in the digital tomosynthesis for pulmonary imaging. Eur Radiol 5:96–101
7. Ghosh Roy DN, Kruger RA, Yih B et al (1985) Selective plane removal in limited angle tomographic imaging. Med Phys 12:65–70
8. Matsuo H, Iwata A, Horiba I et al (1993) Three-dimensional image reconstruction by digital tomosynthesis using inverse filtering. IEEE Trans Med Imaging 12:307–313
9. Knutsson HE, Edholm P, Granlund HG et al (1980) Ectomography—a new radiographic reconstruction method I theory and error estimates. IEEE Trans Biomed Eng 27:640–648
10. Petersson CU, Edholm P, Granlund HG et al (1980) Ectomography—a new radiographic reconstruction method II computer-simulated experiments. IEEE Trans Biomed Eng 27:649–655
11. Chakraborty DP, Yester MV, Barnes GT et al (1984) Self-masking subtraction tomosynthesis. Radiology 150:225–229
12. Ruttiman UE, Groenhuis RA, Webber RL (1984) Restoration of digital multi-plane tomosynthesis by a constrained iteration method. IEEE Trans Med Imaging 3:141–148
13. Kolitsi Z, Panayiotakis G, Pallikarakis N (1993) A method for selective removal of out-of-plane structures in digital tomosynthesis. Med Phys 20:47–50
14. Sone S, Kasuga T, Sakai F et al (1993) Chest imaging with dual-energy subtraction digital tomosynthesis. Acta Radiol 34:346–350
15. Michael U, Akram A (1996) A review of wavelets in biomedical application. Proc IEEE 84:626–638
16. Donoho DL, Johnstone JM (1994) Ideal spatial adaptation by wavelet shrinkage. Biometrika 81:425–455
17. Kolaczyk ED (1996) A wavelet shrinkage approach to tomographic image reconstruction. J Am Stat Assoc 91:1079–1090
18. Nitzken M, Bajaj N, Aslan S et al (2013) Local wavelet-based filtering of electromyographic signals to eliminate the electrocardiographic-induced artifacts in patients with spinal cord injury. J Biomed Sci Eng 6:1–13
19. Nitkzen M, Beache G, Elnakib A et al (2012) Improving full-cardiac cycle strain estimation from tagged CMR by accurate modeling of 3D image appearance characteristics. In: Proceedings of IEEE international symposium on biomedical imaging (ISBI'12) Barcelona Spain May 2–5, pp 462–465
20. Badea C, Kolitsi Z, Pallikarakis N (1998) A wavelet method for removal of out-of-plane structures in digital tomosynthesis. Comput Med Imaging Graph 22:309–315
21. Antoniadis A, Gregoire G, Nason G (1999) Density and hazard rate estimation for right-censored data using wavelet methods. J R Stat Soc B 61:63–84
22. Hall P, Penev S, Kerkyacharian G, Picard D et al (1997) Numerical performance of block thresholded wavelet estimators. Stat Comput 7:115–124
23. Donoho DL, Johnstone IM, Kerkyacharian G et al (1996) Density estimation by wavelet thresholding. Ann Stat 24:508–539
24. Ullman G, Dance DR, Sandborg M et al (2010) A monte carlo-based model for simulation of digital chest tomosynthesis. Radiat Prot Dosim 139:159–163

25. Svalkvist A, Bath M (2010) Simulation of dose reduction in tomosynthesis. Med Phys 37:258–269
26. Bath M, Hakansson A, Tingberg A et al (2005) Method of simulating dose reduction for digital radiographic systems. Radiat Prot Dosimetry 114:253–259
27. Mathworks Inc (2011) MATLAB. http://www.mathworks.com/products/matlab/
28. Kak AC, Slaney M (2001) Principles of computerized tomographic imaging. Classics in Applied Mathematics 33. (SIAM, Philadelphia)
29. Kume Y, Doi K, Ohara K et al (1986) Investigation of basic imaging properties in digital radiography. 10. Structure mottle of II-TV digital imaging. Med Phys 13:843–849
30. Giger ML, Ohara K, Doi K (1986) Investigation of basic imaging properties in digital radiography. 9. Effect of displayed grey levels on signal detection. Med Phys 13:312–318
31. Kasap S, Frey JB, Belev G et al (2011) Amorphous and polycrystalline photoconductors for direct conversion flat panel x-ray image sensors. Sensors (Basel) 11:5112–5157
32. Mallat S, Zhong S (1992) Characterization of signals from multiscale edges. IEEE Trans Pattern Anal Mach Intell 14:710–732
33. Daubechies I (1988) Orthonormal bases of compactly supported wavelets. Commun Pure Appl Math 41:909–996
34. Mathworks Inc (2011) Wavelet toolbox. http://www.mathworks.com/products/wavelet/
35. Yamada Y, Jinzaki M, Hasegawa I et al (2011) Fast scanning tomosynthesis for the detection of pulmonary nodules. Invest Raiol 46:471–477
36. Tapiovaara M, Siiskonen T (2008) A Monte Carlo program for calculating patient doses in medical x-ray examinations (2nd Ed.). Report No. STUK-A231 STUK Helsinki, Finland
37. Rossmann K (1969) Point spread-function, line spread-function, and modulation transfer function. Radiology 93:257–272
38. Sabol JM (2009) A Monte Carlo estimation of effective dose in chest tomosynthesis. Med Phys 36:5480–5487